1 **Fluorescence lifetime imaging of pH along the secretory pathway**

2 Peter T.A. Linders[1], Melina Ioannidis[2], Martin ter Beest[1] and Geert van den Bogaart[1,2,*]

3

4 [1] Department of Tumor Immunology, Radboud Institute for Molecular Life Sciences, Radboud University Medical

5 Center, 6525 GA Nijmegen, The Netherlands

6 [2] Department of Molecular Immunology, Groningen Biomolecular Sciences and Biotechnology Institute, University

7 of Groningen, 9747AG, Groningen, Netherlands

8 [*] Correspondence: g.van.den.bogaart@rug.nl; Tel.: +31-50-36-35230

9

10 **Abstract**

11 Many cellular processes are dependent on correct pH levels, and this is especially important for the secretory

12 pathway. Defects in pH homeostasis in distinct organelles cause a wide range of diseases, including disorders of

13 glycosylation and lysosomal storage diseases. Ratiometric imaging of the pH-sensitive mutant of green fluorescent

14 protein (GFP), pHLuorin, has allowed for targeted pH measurements in various organelles, but the required

15 sequential image acquisition is intrinsically slow and therefore the temporal resolution is unsuitable to follow the

16 rapid transit of cargo between organelles. We therefore applied fluorescence lifetime imaging microscopy (FLIM)

17 to measure intraorganellar pH with just a single excitation wavelength. We first validated this method by

18 confirming the pH in multiple compartments along the secretory pathway and compared the pH values obtained

19 by the FLIM-based measurements with those obtained by conventional ratiometric imaging. Then, we analyzed the

20 dynamic pH changes within cells treated with Bafilomycin A1, to block the vesicular ATPase, and Brefeldin A, to

21 block ER-Golgi trafficking. Finally, we followed the pH changes of newly-synthesized molecules of the inflammatory

22 cytokine tumor necrosis factor (TNF)-α while they were in transit from the endoplasmic reticulum via the Golgi to

23 the plasma membrane. The toolbox we present here can be applied to measure intracellular pH with high spatial

24 and temporal resolution, and can be used to assess organellar pH in disease models.

25

26 **Keywords**

27 Fluorescent proteins, pHLuorin, Golgi apparatus, Secretory pathway, Fluorescence lifetime imaging microscopy

28 **Introduction**

29   Physiological pH homeostasis is crucial for many cellular processes. Not only the cytosolic pH is of

30   importance, but defined intraorganellar pH delineates the secretory pathway. The pH of the endoplasmic

31   reticulum (ER) is approximately 7, while the Golgi apparatus slightly acidifies from pH 6.7 at the *cis* face to pH 6.0

32   at the *trans* face[1–3]. Before secretory cargo is released at the plasma membrane and reaches the neutral pH of the

33   extracellular environment, the pH in secretory vesicles is about 5.2[1,2].

34   pH is not only crucial for proper protein folding and enzyme activity through influencing the charge of

35   amino acid side chains, but its importance in secretory protein transport is increasingly clear[4]. pH affects binding

36   affinities of cargo molecules to trafficking chaperones, and thereby pH differences facilitate intracellular transport

37   by both influencing the transit of cargo[5–11] and the sorting of secretory pathway resident proteins[12–14]. Moreover,

38   the localization of glycosylation enzymes and their substrates is determined by pH[4,15–18], and defects in this

39   homeostasis cause a wide range of human disease[4,19–25]. Being able to accurately determine intraorganellar pH

40   along the secretory pathway is therefore of both fundamental and diagnostic importance.

41   Fluorescent dyes that allow the measurement of intraorganellar pH exist and are commercially

42   available[26–30], but the inability of specific organellar targeting is a major drawback. The pH in the lumen of the Golgi

43   and ER in mammalian cells have been measured using Shiga-like toxins covalently bound to fluorescent dyes[31,32]

44   and with the biotin-avidin system[33]. However, especially the development of pH-sensitive mutants of green

45   fluorescent protein (GFP), such as pHLuorin[34,35], which can be targeted to specific organelles by fusion proteins,

46   have enabled specific measurement of intracellular compartments. Two classes of pHLuorin were developed by

47   mutagenesis which altered the bimodal excitation spectrum of GFP with peaks at 395 and 475 nm[34,36]. First, ecliptic

48   pHLuorin, which shows a reduction of its excitation efficiency at 475 nm at pH values lower than 6. Second,

49   ratiometric pHLuorin which shows a gradual increase in the ratio of excitation at 475/395 nm between pH 5.5 and

50   pH 7.5[34]. With ecliptic pHLuorin, intraorganellar pH can be determined by first recording an image at 475 nm

51   excitation, and then correlating the fluorescence intensities with a calibration curve. The pH can be determined

52   with ratiometric pHLuorin using a similar approach, but now by sequentially recording images at 395 and 475 nm

53   excitation. A new version of ratiometric pHLuorin, ratiometric pHLuorin2 (RpHLuorin2) was later developed with 8-

54   fold improved fluorescence[35].

55   Ecliptic pHLuorin is less accurate than ratiometric pHLuorin, because the fluorescence intensity not only

56   depends on the pH but also on the concentration of pHLuorin. However, ratiometric imaging also has several

57   drawbacks, such as sensitivity to background fluorescence leading to high variation in the ratio values and the

58   need for two sequential image acquisitions with two different excitation wavelengths. As the exocytic pathway is

59   highly dynamic, the sequential imaging could potentially result in misalignment of the emitted signal,

60   compromising the calculation of ratio values. To overcome this problem of dual excitation, GFP-based probes have

61   been developed that show a pH-dependent change in fluorescence emission, including E^2GFP[37] and deGFP4[38,39],

62   and pH-sensitive fluorophores have been targeted to organelles with the HaloTag technology[40]. However, spectral

63   overlap in fluorescence emission wavelengths limits the use of these probes for multi-color experiments together

64   with other fluorescent probes.

65   In this study, we took another approach to overcome the problem of dual excitation and exploit

66   fluorescence lifetime, an intrinsic property of fluorophores that is insensitive to changes in laser intensity or

67   protein concentration[41,42] but is sensitive to pH[43,44], to accurately measure intraorganellar pH with both high spatial

68   and temporal resolution.

69

70   **Results**

71   *FLIM measurements of recombinant ratiometric pHLuorin2*

72   We first measured the fluorescence excitation spectra of recombinant RpHLuorin2 (Supplementary Figure 1) in

73   different pH solutions with a fluorescence spectrometer. Depending on the pH of the medium, the p-

74   hydroxybenzylidene-imidazolidinone moiety in the chromophore of pHluorin2, a derivative of GFP[35], can exist in

75   either the neutral phenol form or the anionic phenolate form[45]. As expected[34], we observed strong dependence of

76   the excitation efficiencies on pH, as a higher pH resulted in an increased emission brightness (at 508 nm) at an

77   excitation wavelength of 470 nm, whereas the fluorescence brightness was reduced at an excitation wavelength of

78   405 nm (Supplementary Figure 1a). These data show that for pHluorin2, the anionic form shows an excitation peak

79   at 405 nm, while the peak with 470 nm corresponds to the neutral form. We then plotted the ratios of the

80   emission signals with 405 nm over 470 nm excitation as a function of the pH and fitted these data with a dose

81   response relationship, an empirical model to fit the sigmoidal data as the (de)protonation states of RpHLuorin2 will

3

82   saturate at very high and low pH values (Supplementary Figure 1b). The largest changes in fluorescence of

83   RpHLuorin2 were observed between pH 5.5 and pH 7, making RpHLuorin2 an excellent candidate for pH

84   measurements in the secretory pathway.

85   As ratiometric determination of pH with RpHLuorin2 requires two sequential image acquisitions with

86   different excitation wavelengths, we investigated whether fluorescence lifetime imaging microscopy (FLIM) would

87   be an appropriate substitute to allow for single-scan imaging. We hypothesized that as the lifetime of fluorophores

88   is influenced by pH[43,44], the pH sensitivity of RpHLuorin2 would allow for accurate pH measurement based on

89   fluorescence lifetime. Therefore, we performed FLIM of recombinant RpHLuorin2 in different pH solutions at 470

90   nm excitation (Figure 1). For GFP, the fluorescence lifetime of the phenolate form is in the 2–3 ns range, while that

91   of the phenol form is < 100 ps[46,47]. At 470 nm excitation, we will mainly excite the (fast) phenol form, but (due to

92   fluorescence cross-talk) there will also be some contribution of the (slow) phenolate form. The observed

93   fluorescence lifetime can hence be regarded as a mixture of the decays of the neutral and anionic forms. Thus, an

94   increase in pH will result in a net higher lifetime, as has been reported for other GFP-derived fluorescent

95   proteins[43,48].

96   For purified recombinant pHLuorin2, we observed a dependency of the lifetime as a function of pH, and

97   the fluorescence lifetime increased upon an increasing pH (Figure 1). However, the fluorescence lifetime changed

98   over a larger range of pH values (4.5–7.5; Figure 1d) than the ratio of 405/470 nm excitations (5.5–7.5,

99   Supplementary Figure 1b). This larger dynamic range, which is likely caused by a second protonation event, is an

100   advantage of the FLIM-based approach, because it increases the range of pH values that can be determined. We

101   then fused RpHLuorin2 to several intraorganellar markers in the secretory pathway to perform pH measurements

102   in living cells.

103

104   *pH measurements in the secretory pathway*

105   In order to accurately measure intraorganellar pH of specific organelles, we targeted RpHLuorin2

106   intracellularly by fusing it to proteins and targeting sequences that locate to specific subcellular locations in the

107   secretory pathway (Figure 3a). The pH range that can be measured with lifetime-based measurements of

108   pHLuorin2 (4.5–7.5) is ideally suited for measuring pH along the secretory pathway, as the pH is neutral within the

109   ER (~7), slightly acidic (~6) in the Golgi network, and about 5.2 in secretory vesicles[1–3]. To interrogate the luminal

110   pH along the entire secretory pathway, we fused RpHLuorin2 to the signal sequence of the ER-resident protein

111   calreticulin and a C-terminal ER retention signal KDEL for ER targeting, to the luminal regions of *cis-*/medial-Golgi

112   protein alpha-1,6-mannosyl-glycoprotein 2-beta-N-acetylglucosaminyltransferase (MGAT2), to *trans*-Golgi enzyme

113   beta-1,4-galactosyltransferase 1 (GalT), to *trans*-Golgi network protein TGN46, and to lysosome-associated

114   membrane glycoprotein 1 (LAMP1) for lysosomal targeting, and finally to a GPI anchor for plasma membrane (i.e.,

115   extracellular) localization. For the Golgi enzymes (MGAT2 and GalT), we truncated each protein by removing their

116   catalytic sites and only kept the transmembrane region and stalk regions responsible for their localization[49–51].

117   We then expressed the fusion constructs in HeLa cells, and recorded FLIM images. We used the GPI-

118   anchored RpHLuorin2 (GPI-RpHLuorin2) to calibrate the probe expressed in cells using the same pH buffers as used

119   for the calibration of purified RpHLuorin2 (Figure 2). We again observed a dependency of the fluorescence lifetime

120   of RpHLuorin2 on pH, although the absolute fluorescence lifetime values were lower than for the recombinant

121   RpHLuorin2, possibly due to crowding effects leading to fluorescence self-quenching[52]. These crowding effects, as

122   well as intracellular pools of GPI-pHLuorin2, likely also contributed to the variation among cells. The fluorescence

123   lifetime dependency on pH could again be fitted with a sigmoidal dose-response model.

124   After successfully calibrating our system, we proceeded with pH measurements in the lumen of the

125   organelles along of the secretory pathway (Figure 3). With ER-RpHLuorin2, we measured an apparent average pH

126   of 7.2 (95% confidence interval (CI) ± 0.08), while with medial-Golgi marker MGAT2-RpHLuorin2 we measured an

127   apparent average pH of 6.1 (95%CI ± 0.07), and with *trans*-Golgi marker GalT-RpHLuorin2 an apparent average pH

128   of 5.9 (95%CI ± 0.07) (Figure 3b, c). Finally, for lysosomal marker LAMP1-RpHLuorin2 we measured an apparent

129   average pH of 4.7 (95%CI ± 0.15) (Figure 3b, c). These pH values are all consistent with previous literature[1,26]. The

130   fluorescence intensities (numbers of photons collected per cell) did not correlate with the fluorescence lifetimes

131   for the four measured probes (Supplementary Figure 2), indicating that intercellular variations were not caused by

132   differences in expression levels.

133   To compare the FLIM-based measurements with ratiometric measurements, we also performed

134   ratiometric imaging in cells using confocal laser-scanning microscopy where we changed the excitation wavelength

135   each line of the imaging (Supplementary Figure 3). Confirming our previous experiments with purified RpHLuorin2

136 (Figure 1; Supplementary Figure 1), we observed for GPI-pHluorin2 that the ratio of fluorescence with 405 and 470

137 nm excitations changed over a narrower range of pH values (5.5–7.5; Supplementary Figure 3a) than with FLIM

138 imaging (5.5–7.5; Figure 2). For the MGAT2 and GalT probes, we observed similar pH values as with the FLIM-based

139 measurements (Supplementary Figure 3b; MGAT2 pH 6.5 (95%CI ± 0.16), GalT pH 6.1 (95%CI ± 0.13)). However,

140 the spread of the data was considerably (~2-fold) larger for the ratiometric approach. As a result, less cells have to

141 be analyzed with FLIM-based approach to accurately determine the pH. To illustrate this point, we performed

142 Bootstrap statistical analysis where we sampled our datasets to estimate the 95% CI based on samples of

143 increasing numbers of cells (Supplementary Figure 4). Based on this analysis, we estimate that for the FLIM-based

144 approach >16 cells needed to be measured for an accurate estimation of the pH for the ER, MGAT2, GalT and

145 LAMP1 markers. However, for the ratiometric approach, approximately 2-fold more cells needed to be analyzed to

146 reach a similar 95%CI.

147 To further characterize the RpHLuorin2 FLIM system, we challenged cells with the vacuolar H^+-ATPase (V-

148 ATPase) inhibitor Bafilomycin A1 (BafA1)[53]. The mammalian V-ATPase is a protein pump that acidifies

149 intraorganellar lumina by translocating protons across the membrane[54,55]. Our experiments with the MGAT2 and

150 GalT probes showed that challenging the cells for 1 hr with 200 nM BafA1 resulted in a reduced acidification of

151 both the cis- and trans-Golgi apparatus, although this perturbation was incomplete as the pH did not reach

152 completely neutral values (Figure 4). Taken together, our data show that the RpHLuorin2 FLIM system is highly

153 suitable for intracellular pH measurements with only a single image acquisition.

154

155 *Dynamic measurements of pH in the secretory pathway*

156 To evaluate whether our method would be able to measure dynamic changes in pH, we started by

157 measuring the pH of the medial-Golgi marker MGAT2-pHLuorin2 in the presence of fungal metabolite Brefeldin A

158 (BFA). BFA is a potent inhibitor of ER-Golgi trafficking and causes the relocation of Golgi-resident enzymes to the

159 ER[56,57]. We therefore expected a substantial increase in pH when MGAT2-RpHLuorin2 expressing cells were

160 challenged with BFA. Indeed, we measured an apparent average pH of 7.1 (95%CI ± 0.07) in the BFA-challenged

161 cells compared to an apparent average pH of 6.4 (95%CI ± 0.08) in the vehicle control cells (Figure 5a, b). This

162 result means that our system is capable of measuring dynamic alterations of pH in living cells.

163   Next, we employed FLIM-based measurements to monitor the changes of the pH in real-time along the

164   secretory pathway. To this end, we chose the secreted cytokine tumor necrosis factor alpha (TNF-α) as a model

165   protein that is transported through the secretory pathway. Using the Retention Using Selective Hooks (RUSH)

166   system[51], we synchronized the transit of TNF-α along the secretory pathway. RUSH uses the expression of two

167   separate constructs in the cell: (i) the hook construct, which is an ER-targeting sequence fused to streptavidin, and

168   (ii) the reporter construct which is the protein of interest (i.e., TNF-α) fused in tandem to a streptavidin binding

169   protein (SBP) and a fluorescent protein (RpHLuorin2). When biotin is absent from the culture medium, the reporter

170   construct is held at the ER through an interaction of streptavidin of the hook construct and the SBP. When biotin is

171   added to the culture medium, biotin outcompetes this interaction and the reporter construct is released and

172   transits along the secretory pathway in a synchronized fashion.

173   In our case, we used the KDEL-motif as a targeting sequence for the ER[51], and used a TNFα-SBP-

174   RpHLuorin2 fusion protein (RUSH TNFα-SBP-RpHLuorin2) as the reporter construct, so that we could follow the

175   dynamic transit of TNF-α from the ER to the plasma membrane (Figure 5c-e, Supplementary Movie 1). We

176   confirmed the subcellular localizations with immunolabeling experiments where we fixed cells expressing TNFα-

177   SBP-RpHLuorin2 at discrete time intervals after biotin addition and immunolabeled for organellar markers for the

178   ER (PDI), Golgi network (GM130) and plasma membrane (WGA) (Supplementary Figure 5).

179   In the absence of biotin in the cell culture medium, when all the TNFα-SBP-RpHLuorin2 reporter construct

180   was trapped within the ER, we measured an apparent average pH of 7.58 (95%CI ± 0.46) (Figure 5c-e,

181   Supplementary Movie 1). In the ~25 min following the addition of biotin to the cells, TNFα-SBP-RpHLuorin2 was

182   trafficked through the Golgi and the apparent average pH gradually decreased to around pH 6. At later time points,

183   the pH gradually increased again as more TNFα-SBP-RpHLuorin2 reached the plasma membrane. As HeLa cells

184   express the protease TACE, TNF-α likely dissociates from the plasma membrane[58–60].

185   After biotin addition, the TNF-α-RpHLuorin2 became concentrated in the Golgi network, leading to a local

186   increase of signal at this position. In order to not saturate the signal at this timepoint, we had to use a low intensity

187   of excitation light for the RUSH experiments. However, at the start of the experiments (i.e., prior to biotin

188   addition), the TNF-α-RpHLuorin2 construct was located at the ER, which in mammalian cells is diffuse and

189   scattered through the entire cytoplasm. Likely as a consequence, the photon count/pixel at earlier timepoints was

190   low leading to an overestimation of the pH particularly for the ER localization. Also because of the limited number

191   of photons, we fitted the fluorescence lifetime histograms with a single exponential decay function and report the

192   apparent average pH per cell[61].

193   This result demonstrates that FLIM-based pH measurements are a suitable method to determine

194   intraorganellar pH with high temporal resolution.

195

196   **Discussion**

197   In this study, we measured the pH in various subcellular compartments using FLIM of the pH-sensitive

198   fluorescent protein RpHLuorin2. Consistent with previous literature, we observed a clear acidification of luminal

199   pH through the secretory pathway[1–3]. The fusion of RpHLuorin2 is not restricted to the proteins we described here;

200   this system is applicable to any other intraorganellar measurement, provided RpHLuorin2 can be fused to a luminal

201   domain of a protein residing in the target organelle. Furthermore, additional applications include combining

202   RpHLuorin2 with other fluorescence (lifetime) based probes to measure pH and other cellular processes

203   simultaneously within the same cell.

204   We also show that the FLIM approach enables to measure pH with a kinetic resolution high enough to

205   follow the dynamic transit of a cargo molecule along the secretory pathway. In this respect, our approach

206   complements measurements of the exocytic pathway using Vero and Shiga toxins labeled with-pH sensitive

207   fluorophores[31]. These toxins are endocytosed by receptor-mediated endocytosis and then transit via the Golgi

208   network to the ER, a process which can be followed by microscopy. While this approach also enables to measure

209   pH along the secretory pathway, a disadvantage is that it does not allow to follow the pH of designated secretory

210   targets. For example, after transit through the Golgi, TNF-α is reported to traffic via designated sub-compartments

211   of recycling endosomes to the plasma membrane[62], and it is not known whether Shiga toxins also traffic via these

212   compartments.

213   Compared to excitation-based ratiometric imaging, the key improvement of our study is the usage of

214   FLIM. Ratiometric imaging of pHLuorin and derivatives[30,34,35] requires the sequential recording of the fluorescent

215   protein at both 405 and 470 nm excitation wavelengths, while the emission is recorded at the same wavelength.

216   Although certain optical schemes such as split-beam excitation might facilitate fast switching between excitation

217   wavelengths, this sequential excitation intrinsically limits the temporal resolution and consequently limits the

218   applicability for pH determination in dynamically moving and reshaping organelles. FLIM mitigates this issue, as

219   only a single recording with a single excitation wavelength is required. Moreover, FLIM measurements are not

220   dependent on laser intensity[41,42], while ratiometric measurements can easily be affected by fluctuations in

221   excitation laser power. FLIM measurements are thus more comparable between experiments, as supported by our

222   findings that the spread in the data is larger for the ratiometric than for the FLIM approach. Another advantage of

223   the FLIM-based approach is that reference measurements can be used over independent experiments, because

224   the fluorescence lifetime is independent of the fluorescence intensity[41,42]. This is an advantage over the ratiometric

225   approach, where small differences in the laser intensity and alignment of the microscope can have a major effect.

226   However, a disadvantage is that it requires access to a FLIM microscope, whereas ratiometric imaging can be

227   performed on most confocal and epifluorescence microscopes.

228   In contrast to another study which relies on equilibrating pH with the ionophore monensin[30], we used

229   GPI-anchored RpHLuorin2 to obtain calibration curves with defined pH buffers, because monensin is a known

230   inhibitor of physiological Golgi transport, thereby likely affecting the observed fluorescence lifetime values[63–69].

231   Defects in the regulation of pH are a hallmark of a wide range of disease, including disorders of

232   glycosylation[4,19,21–25], cancer[70], neurodegenerative diseases[71–74], mitochondrial disorders[75] and lysosomal storage

233   disorders[76]. The tools we presented in this study offer a method to assess intraorganellar pH using FLIM. Our data

234   show that FLIM is more accurate than ratiometric imaging. Moreover, due to its high temporal resolution, it not

235   only enables to measure pH in static compartments, but also to measure the dynamic changes that a protein

236   experiences during its trafficking along the secretory pathway.

237

248   **Author Contributions**

249   P.T.A.L., M.t.B., and G.v.d.B. designed and performed the experiments and wrote the paper. M.I. performed the

250   ratiometric pH measurements in HeLa cells and contributed to the writing of the paper.

251   **Declaration of Interests**

252   The authors declare that they have no competing financial interests.

253   **Methods**

254   *Cloning*

255   The sequence of RpHLuorin2[35] was synthesized by Genscript for both recombinant (codon optimized for *E. coli*)

256   and mammalian cell expression. Synthetic RpHLuorin2 codon optimized for *E. coli* for recombinant protein

257   production was inserted in pET-28a(+) (EMD Biosciences) with restriction sites NdeI and XhoI. The construct for

258   cytosolic expression of RpHLuorin2 was generated by replacing EGFP in pEGFP-N1 (Clontech) with synthesized

259   RpHLuorin2 using restriction sites AgeI and BsrGI. ER-targeting of RpHLuorin2 was achieved by inserting the signal

260   sequence of calreticulin (MLLSVPLLLGLLGLAVA) and flexible GGSGGS linker before RpHLuorin2 and adding a KDEL

261   motif for luminal ER retention after RpHLuorin2. Targeting to the MGAT2-positive compartment was achieved by

262   inserting synthetic truncated MGAT2 (residues 1-89 of Uniprot Q10469, Genscript) in the vector for cytosolic

263   expression of RpHLuorin2 with restriction sites EcoRI and BamHI. The starting codon of RpHLuorin2 was removed

264   and a flexible GGSGGS linker was added between the two protein fragments. Targeting to the GalT-positive

265   compartment was achieved by inserting truncated GalT (Addgene plasmid #87325) in the vector for cytosolic

266   expression of RpHLuorin2 with restriction sites SmaI and BamHI. The starting codon of RpHLuorin2 was removed

267   and a flexible GGSGGS linker was added between the two protein fragments. Targeting to LAMP1-positive

268   compartments was achieved by inserting the signal sequence of LAMP1 (LAMP1-mGFP[77], Addgene plasmid

269   #34831) N-terminal to RpHLuorin2 with restriction sites HindIII and AgeI. Then, the luminal domain of LAMP1 was

270   placed C-terminal to RpHLuorin2 after a flexible GSGS linker with restriction sites BsrGI and NotI. GPI-RpHLuorin2

271   was generated by replacing mRFP from GPI-mRFP with synthetic RpHLuorin2 with restriction sites XmaI and NotI.

272   RUSH TNFα-RpHLuorin2 was generated by replacing EGFP from Str-KDEL_TNF-SBP-EGFP (Addgene plasmid #65278)

273   with synthetic RpHLuorin2 (Genscript) with restriction sites SbfI and BsrGI. All sequences were verified by Sanger

274   sequencing prior to transfection. All generated plasmids from this study have been deposited at Addgene.

275

276   *Cell culture and transfection*

277   HeLa cells (authenticated by ATCC through their human STR profiling cell authentication service) were maintained

278   in high glucose DMEM with Glutamax (Gibco 31966021), supplemented with 10% fetal calf serum (FCS, Greiner

11

279 Bio-one, Kremsmünster, Austria) and antibiotic-antimycotic solution (Gibco 15240-062). Cells were regularly tested

280 for mycoplasma contamination. HeLa cells were transfected with plasmid vectors using Fugene HD (Promega

281 E2311), using the recommended protocol of the manufacturer. Cells were imaged 48 hours post-transfection. Only

282 cells expressing low to moderate levels of the transfected plasmids, based on fluorescence intensity and manual

283 localization scoring, were chosen for subsequent microscopic analyses.

284

285

286 *pH calibration buffers*

287 Buffers with defined pH for the generation of a calibration curve were prepared as described previously[30].

288 Calibration buffers contain 125 mM KCl, 25 mM NaCl, and 25 mM N-[2-hydroxyethyl]-piperazine-N-[2-

289 ethanesulfonic acid] (HEPES, pH 7.5 or 7.0) or 25 mM 2-[N-morpholino] ethanesulfonic acid (MES, pH 6.5, 6.0, 5.5,

290 5.0 or 4.5). Each buffer solution was adjusted to the appropriate final pH using 1 M NaOH or 1 M HCl at 37°C.

291

292 *Recombinant protein expression and purification*

293 RpHLuorin2 in pET-28(a)+ vector was transformed in BL21(DE3) *E. coli*. Cells were grown in 2x yeast extract -

294 tryptone medium and induced with 250 µg/mL β-D-1-thiogalactopyranoside (IPTG) at an OD600 of 0.8 for 2 hrs at

295 37°C and 200 rpm. Cells were pelleted at 3000 × g at 4°C for 30 mins and subsequently lysed with B-PER (Thermo

296 Scientific) supplemented with 50 U DNAseI, 1:500 lysozyme and protease inhibitor cocktail (Roche). Lysates were

297 then cleared by centrifugation (20,000 × g at 4°C for 10 mins) and supernatants with recombinant protein were

298 loaded onto nickel – nitrilotriacetic acid (Ni-NTA) bead columns. Ni-NTA beads were then washed five times with

299 10 mM Tris-HCl pH 7.6 and 150 mM KCl, and proteins were eluted in 10 mM Tris-HCl pH 7.6, 150 mM KCl and 200

300 mM imidazole. To remove the elution buffer, purified protein was dialyzed overnight against ddH$_2$O using 2 mL

301 Slide-A-Lyzer 10K MWCO tubes (Thermo Scientific). Protein concentration was determined using the Micro BCA

302 Protein Assay Kit (Thermo Scientific). Fluorescence of recombinant pHLuorin2 in each pH calibration buffer was

303 measured using Eppendorf semimicro Vis Cuvettes on an LS 55 Fluorescence spectrometer (PerkinElmer). A xenon

304 lamp was used as the excitation source. Samples were excited at 405 and 470 nm, and the emission was recorded

305 at 508 nm.

12

306

Confocal microscopy

Imaging of cells took place in Leibovitz's L-15 medium, with the exception of the samples for the pH calibration curve and the recombinant protein measurements. GPI-RpHLuorin2 and recombinant RpHLuorin2 (10 µM) measurements were performed in the pH buffers mentioned above. For calibration with GPI-RpHLuorin2, cells were preincubated in pH buffer for 15 mins at 37°C to achieve sufficient pH equilibration. For the Bafilomycin A1 assay, cells were treated with 200 nM Bafilomycin A1 (Cayman Chemicals) in DMSO for 1 hour prior to live imaging. For the Brefeldin A assay, cells were treated with 10 µg/mL Brefeldin A (Cayman Chemicals) in DMSO for 15 mins prior to live imaging. Imaging was performed on a Leica SP8 SMD system at 37°C, equipped with an HC PL APO CS2 63x/1.20 WATER objective. pHLuorin2 was excited at 488 nm with a pulsed white light laser, operating at 80 MHz. Photons were collected for one minute or 30 seconds for time-lapse experiments with a HyD detector set at 502 – 530 nm and lifetime histograms of the donor fluorophore were fitted with a monoexponential decay function convoluted with the microscope instrument response function in Leica LAS X. For reconstructing the images, tiff files with τ values were generated using FLIMFit[78] and 2 x 2 spatial binning, and then convoluted with the fluorescent intensities using a custom-written ImageJ macro. Ratiometric pH measurements were done similarly to the FLIM measurements, but instead the imaging was performed on a Leica SP8 SMD system at 37°C, equipped with an HC PL APO CS2 63x/1.20 Water objective or a Zeiss LSM800 system at 37°C, equipped with a Plan Apochromat 1.4x Oil objective. RpHLuorin2 was excited at 405 nm and 488 nm sequentially, images were acquired with an emission wavelength bandwidth (495–560 nm) that included the emission wavelength of 508 nm.

Colocalization analysis

25.000 were plated on cleaned 12 mm glass coverslips (Electron Microscopy Services), transfected as described above with RUSH TNFα-RpHLuorin2. The RUSH assay was performed after 48 hours, and cells were fixed with 4% paraformaldehyde for 15 mins at room temperature at the indicated times and quenched with 50 mM NH$_4$Cl in PBS for 10 mins. Wheat germ agglutinin (WGA) staining was performed without permeabilization and before any other staining step. Briefly, cells were washed with Carbo-Free Blocking Solution (Vector Laboratories, supplemented with 1 mM MgCl$_2$ and CaCl$_2$) and incubated with 4 µg/mL biotinylated WGA (Vector Laboratories)

13

333   diluted in Carbo-Free Blocking Solution. Cells were then incubated with Strepatividin-Alexa Fluor 647

334   (ThermoScientific). Anti-GM130, anti-PDI and anti-GFP (recognizes RpHLuorin2) was performed with

335   permeabilization. Cells were permeabilized and blocked in 2% normal donkey serum (Rockland) and 0.1% saponin

336   (permeabilization buffer) for 30 mins at RT. Primary antibodies were diluted in permeabilization buffer and

337   incubated for 1 h at room temperature: mouse anti-PDI (clone RL90, Novus Biologicals), 10 µg/mL; mouse anti-

338   GM130 (clone 35/GM130, BD Biosciences), 2.5 µg/mL, and rabbit anti-GFP (Rockland), 20 µg/mL. Secondary

339   antibodies were also diluted in permeabilization buffer and incubated for 1 h at room temperature: donkey-anti-

340   rabbit Alexa Fluor 488 and donkey-anti-mouse Alexa Fluor 647 (both ThermoFisher, 5 µg/mL). Cells were finally

341   washed with 0.1% Triton X-100 in PBS to remove any background staining and mounted usin mounting medium

342   with 0.01% Trolox (6-hydroxy-2,5,7,8-tetramethylchroman-2-carboxylic acid) and 68% glycerol in 200 mM sodium

343   phosphate buffer at pH 7.5 with 0.1 µg/mL DAPI (4,6-diamidino-2-phenylindole). Coverslips were sealed with nail

344   polish. Cells were imaged on a Leica SP8 SMD confocal laser scanning microscope, equipped with an HC PL APO

345   CS2 63x/1.20 WATER objective. Colocalization analysis was performed using the *pearsonr* function from the Python

346   package SciPy[79]. Individual cells were first saved to separate .tiff files with ImageJ, and then processed in a fully

347   automated and unbiased fashion using the *pearsonr* function.

348

349   *Quantification and statistical analysis*

350   All mean values represent the average of all cells analyzed. pH calibration curves were fitted with an emperical

351   dose response function as described by equation (1) with the *MM.3* function from the R package *drc*[80].

352

$$y = c + \frac{d}{1 + (\frac{e}{x})}$$

(1)

353   Where *y* is the fluorescence intensity or lifetime, *x* is the pH and *c, d* and *e* are fit parameters.

354   Bootstrap analyses were performed using R statistical software using the interpolated pH values from all

355   cells measured in the lifetime and ratiometric measurements. Briefly, 95% confidence intervals were determined

356   for random samples of measurements (starting from n=2, up to the number of cells per condition). This process

357   was repeated for 10,000 iterations using the *replicate* function.

14

358   All comparisons were first checked for similar mean and median values and acceptable (< 3x) difference in

359   variance. Statistical analysis of three or more groups was performed using a one-way ANOVA, followed by a post-

360   hoc Tukey's honestly significant difference test. $p < 0.05$ was considered significant. *$p < 0.05$, **$p < 0.01$, ***$p <$

361   0.001, ****$p \leq 0.0001$. All statistical analyses were performed using R statistical software. All numerical data were

362   visualized using R package *ggplot2*[81], with violins representing the overall distribution of the data and means ± 95%

363   CI overlaid.

364

365   *Data and code availability*

366   All raw data, including R scripts and ImageJ macros, have been deposited to Zenodo.

367   **Figures**
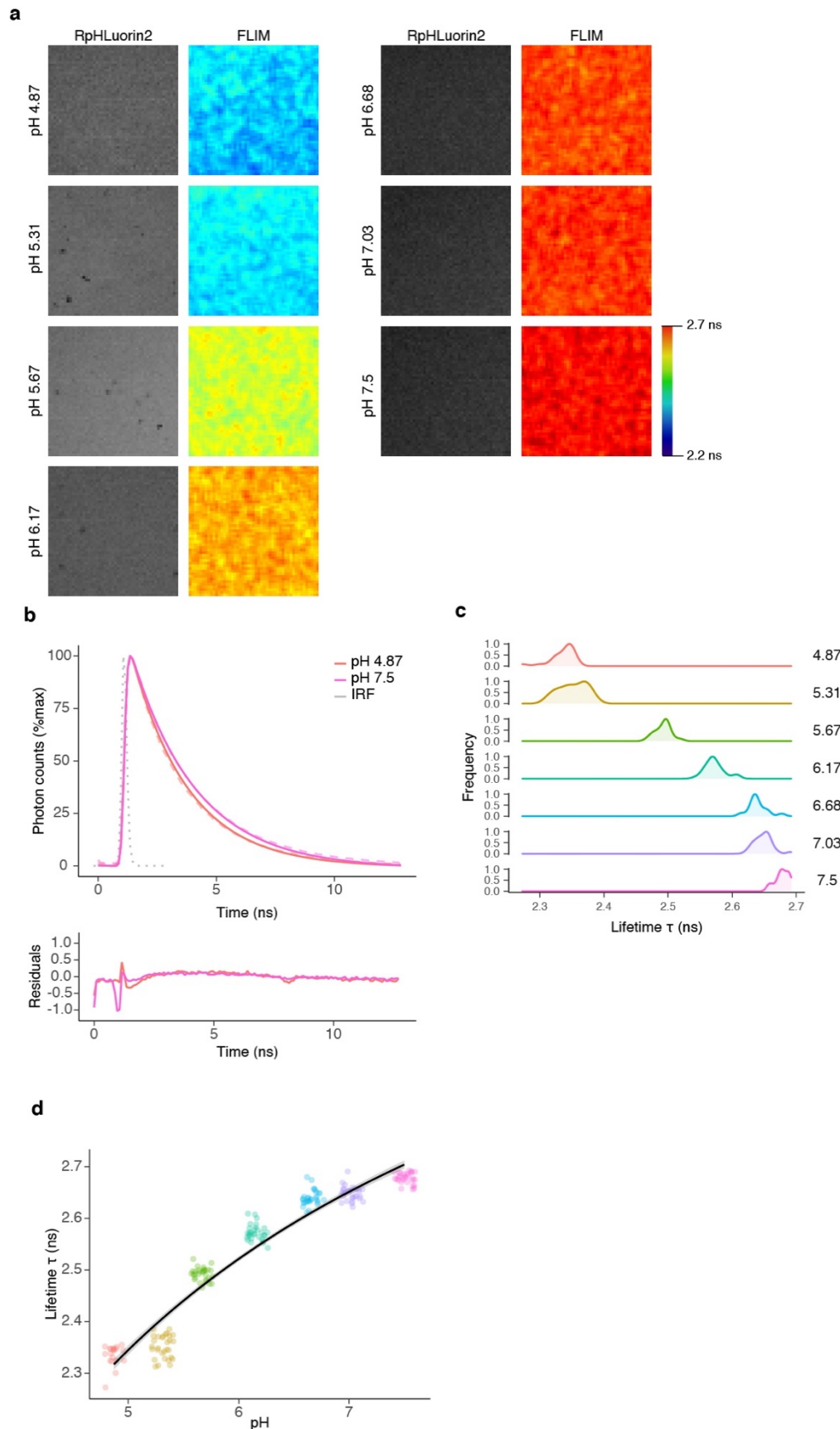
368 **Figure 1. Fluorescence lifetime imaging microscopy (FLIM) of recombinant RpHLuorin2.**

369   (a)   Representative confocal images of 10 μM recombinant RpHLuorin2 in calibration buffers with defined pH.

370   The intensity image (left column) was convoluted with the fluorescent lifetime value per pixel and

371   pseudo-colored (right column).

372   (b)   Representative fluorescence lifetime histograms of recombinant RpHLuorin2 in pH 4.87 solution (red

373   dashed line) or pH 7.5 solution (pink dashed line). Fits with mono-exponential decay functions (pH 4.87,

374   solid red line; pH 7.5, solid pink line) convoluted with the instrumental response function (IRF, gray dotted

375   line). Graphs are normalized to the maximum photon counts.

376   (c)   Average lifetime histograms from the images of panel (a). 30 regions of interest were selected per pH

377   buffer and the average lifetime τ was measured.

378   (d)   pH dependence of recombinant RpHLuorin2 in defined pH calibration buffers from the images of panel
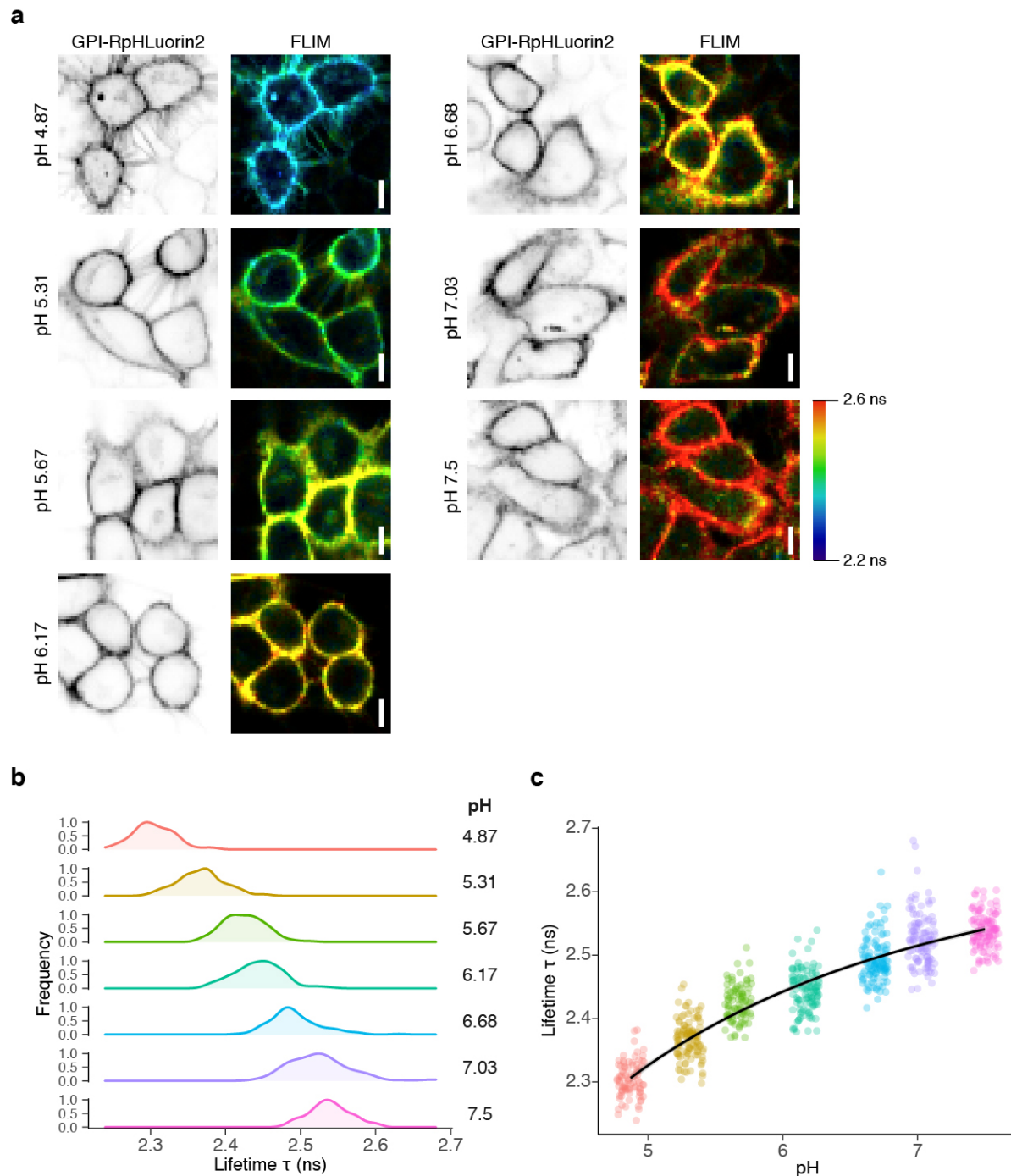
379   (a).

380

Figure 2. Calibration of RpHLuorin2 by fluorescence lifetime imaging microscopy (FLIM) in HeLa cells expressing GPI-RpHLuorin2.

(a) Representative confocal micrographs of HeLa cells expressing GPI-RpHLuorin2 in defined calibration buffers. The intensity image (left column) was convoluted with the fluorescent lifetime value per pixel and pseudo-colored (right column). Scalebars, 10 μm.

19

387   (b) Average lifetime histograms from the images of panel (a). N = 86 (pH 4.87), 108 (pH 5.31), 90 (pH 5.67),

388   115 (pH 6.17), 122 (pH 6.68), 113 (pH 7.03) and 120 (pH 7.5) cells from three independent experiments.

389   (c) pH dependence of HeLa cells expressing GPI-RpHLuorin2 in defined pH calibration buffers from the

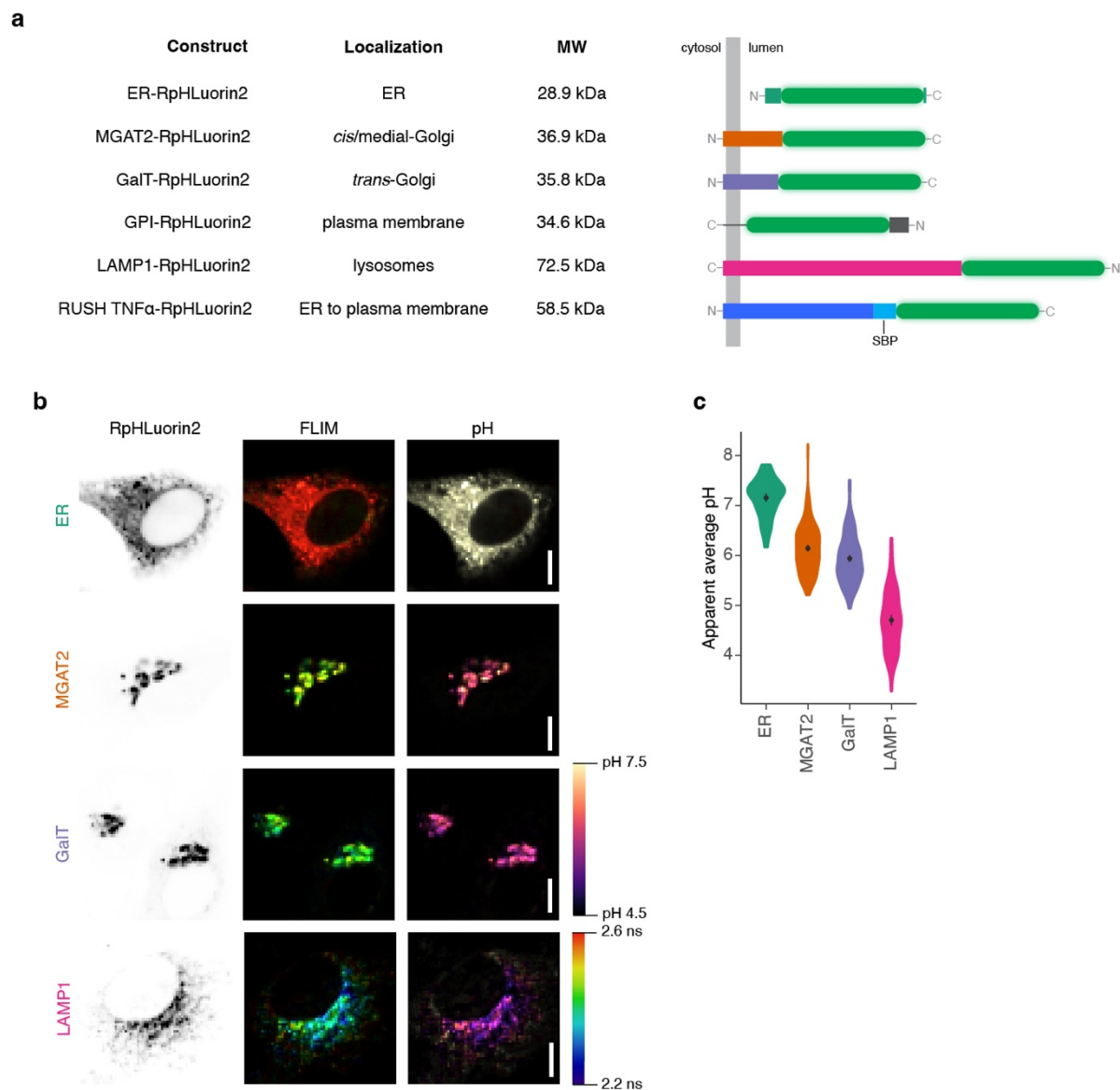390   images of panel (a).

391

Figure 3. Steady-state pH measurements of secretory pathway markers.

(a) Schematic overview of all RpHLuorin2 constructs used in this study. The signal sequence of LAMP1 is removed following co-translational ER insertion and is not shown in the diagram. MW, molecular weight. RUSH, retention using selective hooks[43]. SBP, streptavidin binding protein.

(b) Representative confocal micrographs of HeLa cells expressing the mentioned RpHLuorin2 fusion constructs. The intensity image (left column) was convoluted with the fluorescent lifetime value per pixel and pseudo-colored (middle column). The intensity image was also convoluted with the calculated pH per

21

400   pixel and pseudo-colored (right column). FLIM, fluorescence lifetime imaging microscopy. Scalebars, 10

401   μm.

402   (c) Quantification of average pH values from panel (b). N = 88 (ER), 188 (MGAT2), 193 (GalT), and 134

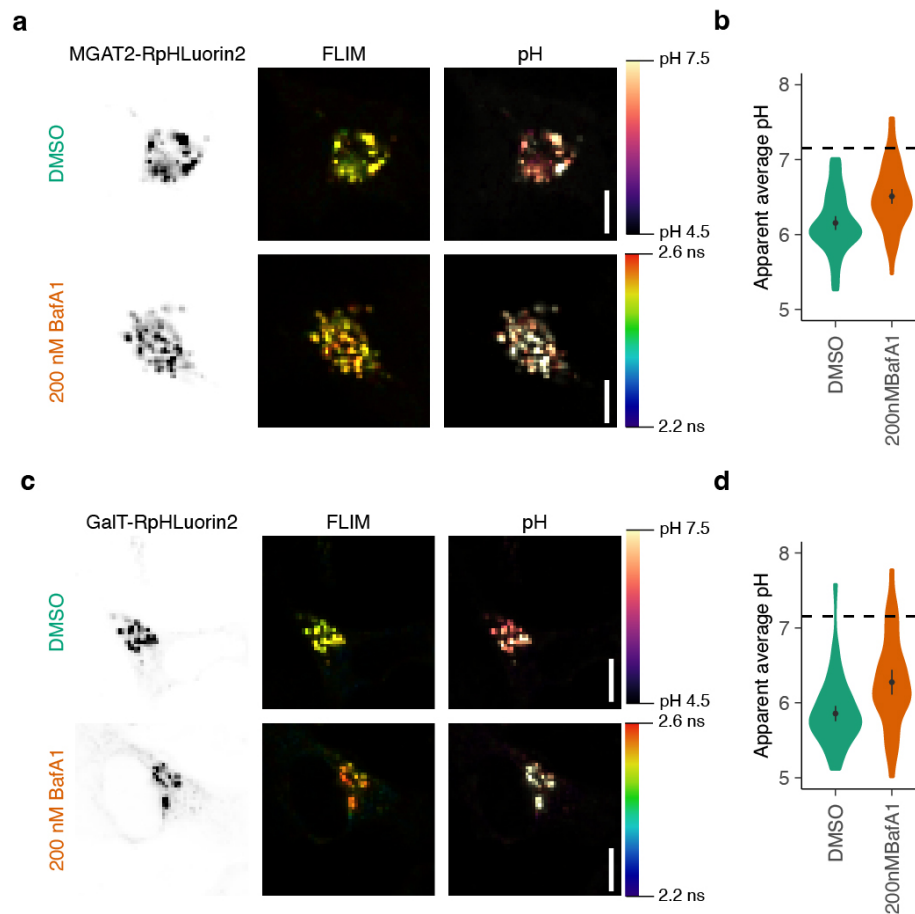403   (LAMP1) cells from 3 – 5 independent experiments.

404

Figure 4. Incomplete blockage of Golgi acidification by Bafilomycin A1.

(a) Representative confocal micrographs of HeLa cells expressing MGAT2-RpHLuorin2 incubated for 1 hr in the absence (solvent control DMSO) or presence of Bafilomycin A1 (200 nM BafA1). To generate the FLIM (fluorescence lifetime imaging microscopy) images (middle column), the intensity images (left column) were convoluted with the fluorescent lifetime value per pixel and pseudo-colored. To generate the pH images, the lifetimes were converted to the calculated pH per pixel and also convoluted with the fluorescence intensities (right column). Scalebars, 10 μm.

(b) Quantification of average pH values from panel (a). N = 72 (DMSO) and 77 (BafA1) cells from 4 independent experiments. The dashed lines indicate the average pH of the ER from Figure 3c.

(c-d) Same as panels (a-b), but now for GalT-RpHLuorin2. N = 68 (DMSO) and 50 (BafA1A) cells from 4 independent experiments.

418

419

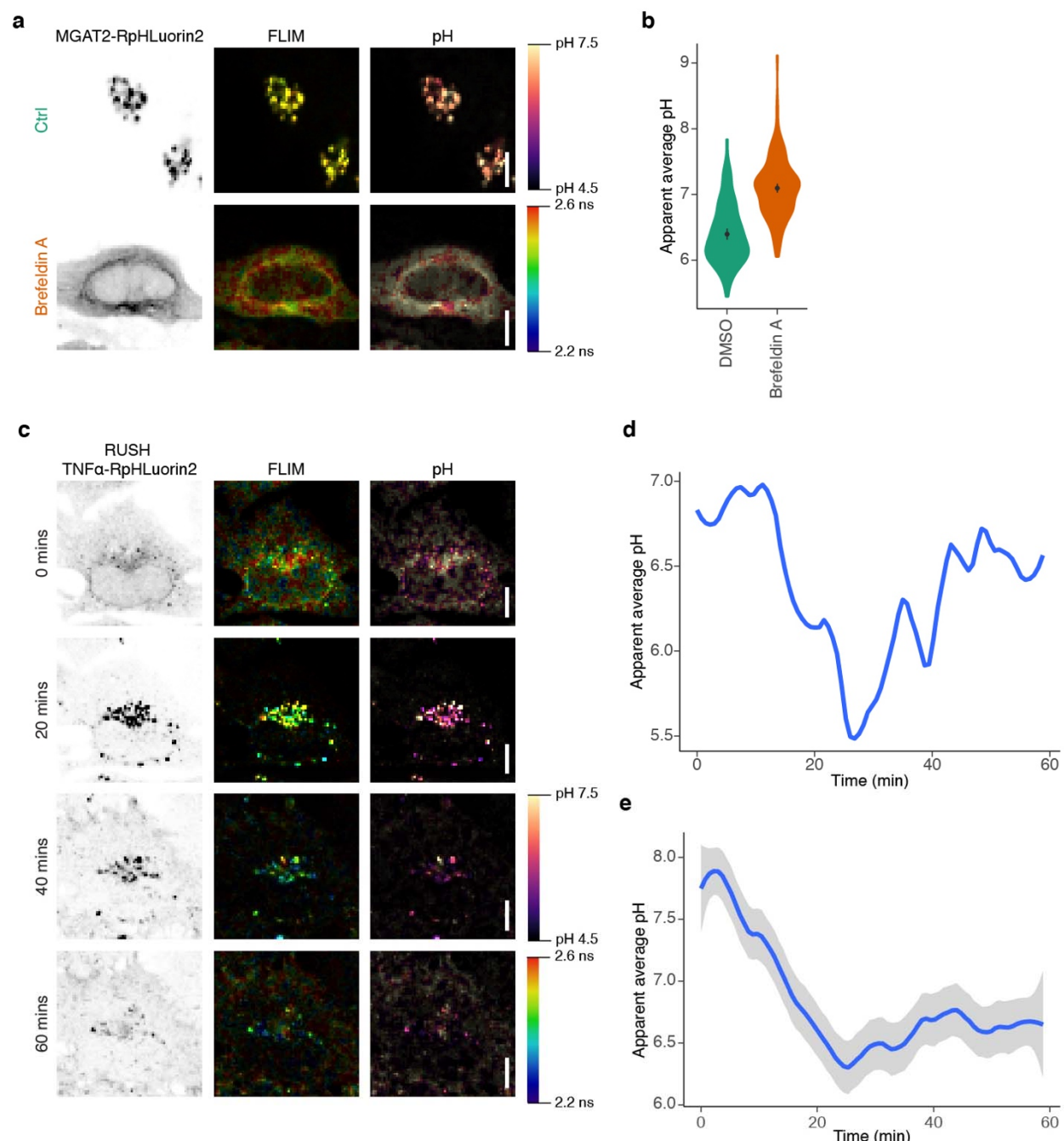420   **Figure 5. Dynamic pH measurements along the secretory pathway.**

421   (a) Representative confocal micrographs of HeLa cells expressing MGAT2-RpHLuorin2 in the absence (Ctrl,

422   green) or presence of Brefeldin A (orange). The intensity image (left column) was convoluted with the

423   fluorescent lifetime value per pixel and pseudo-colored (middle column). The intensity image was also

424   convoluted with the calculated pH per pixel and pseudo-colored (right column). FLIM, fluorescence

425   lifetime imaging microscopy. Scalebars, 10 μm.

426   (b) Quantification of average pH values from panel (a). N = 110 (DMSO) and 165 (Brefeldin A) cells from 2 – 3

427   independent experiments.

428   (c) Representative confocal micrographs of HeLa cells expressing RUSH TNFα-RpHLuorin2 in the absence of

429   biotin (0 min) or 20, 40 and 60 minutes after biotin addition. The intensity image (left column) was

430   convoluted with the fluorescent lifetime value per pixel and pseudo-colored (middle column). The

431   intensity image was also convoluted with the calculated pH per pixel and pseudo-colored (right column).

432   FLIM, fluorescence lifetime imaging microscopy. Scalebars, 10 μm. See also Supplementary Movie 1.

433   (d) Quantification of average pH values of the cell shown in panel (c) and Supplementary Movie 1.

434   (e) Average pH measured of all cells expressing RUSH TNFα-RpHLuorin2. N = 29 from 2 independent

435   experiments.

436

25

437   **References**

438   1.   Casey, J. R., Grinstein, S. & Orlowski, J. Sensors and regulators of intracellular pH. *Nat.*
439   *Rev. Mol. Cell Biol.* **11**, 50–61 (2010).
440   2.   Paroutis, P., Touret, N. & Grinstein, S. The pH of the Secretory Pathway: Measurement,
441   Determinants, and Regulation. *Physiology* **19**, (2004).
442   3.   Schapiro, F. B. & Grinstein, S. Determinants of the pH of the Golgi complex. *J. Biol.*
443   *Chem.* **275**, 21025–32 (2000).
444   4.   Linders, P. T. A., Peters, E., ter Beest, M., Lefeber, D. J. & van den Bogaart, G. Sugary
445   Logistics Gone Wrong: Membrane Trafficking and Congenital Disorders of Glycosylation. *Int. J.*
446   *Mol. Sci.* **21**, 4654 (2020).
447   5.   Appenzeller-Herzog, C., Roche, A.-C., Nufer, O. & Hauri, H.-P. pH-induced conversion of
448   the transport lectin ERGIC-53 triggers glycoprotein release. *J. Biol. Chem.* **279**, 12943–50 (2004).
449   6.   Vavassori, S. *et al.* A pH-Regulated Quality Control Cycle for Surveillance of Secretory
450   Protein Assembly. *Mol. Cell* **50**, 783–792 (2013).
451   7.   Sannino, S. *et al.* Progressive quality control of secretory proteins in the early secretory
452   compartment by ERp44. *J. Cell Sci.* **127**, 4260–4269 (2014).
453   8.   Watanabe, S., Harayama, M., Kanemura, S., Sitia, R. & Inaba, K. Structural basis of pH-
454   dependent client binding by ERp44, a key regulator of protein secretion at the ER–Golgi
455   interface. *Proc. Natl. Acad. Sci.* **114**, E3224–E3232 (2017).
456   9.   Caplan, M. J. *et al.* Dependence on pH of polarized sorting of secreted proteins. *Nature*
457   **329**, 632–635 (1987).
458   10.   Kokkonen, N. *et al.* Defective acidification of intracellular organelles results in aberrant
459   secretion of cathepsin D in cancer cells. *J. Biol. Chem.* **279**, 39982–39988 (2004).
460   11.   Kamiya, Y. *et al.* Molecular Basis of Sugar Recognition by the Human L-type Lectins
461   ERGIC-53, VIPL, and VIP36. *J. Biol. Chem.* **283**, 1857–1861 (2008).
462   12.   Bräuer, P. *et al.* Structural basis for pH-dependent retrieval of ER proteins from the Golgi
463   by the KDEL receptor. *Science* **363**, 1103–1107 (2019).
464   13.   Wilson, D. W., Lewis, M. J. & Pelham, H. R. pH-dependent binding of KDEL to its receptor
465   in vitro. *J. Biol. Chem.* **268**, 7465–7468 (1993).
466   14.   Shibuya, A., Margulis, N., Christiano, R., Walther, T. C. & Barlowe, C. The Erv41–Erv46
467   complex serves as a retrograde receptor to retrieve escaped ER proteins. *J. Cell Biol.* **208**, 197–
468   209 (2015).
469   15.   Rivinoja, A., Hassinen, A., Kokkonen, N., Kauppila, A. & Kellokumpu, S. Elevated Golgi pH
470   impairs terminal N-glycosylation by inducing mislocalization of Golgi glycosyltransferases. *J.*
471   *Cell. Physiol.* **220**, 144–154 (2009).
472   16.   Hassinen, A. *et al.* Functional Organization of Golgi N- and O-Glycosylation Pathways
473   Involves pH-dependent Complex Formation That Is Impaired in Cancer Cells. *J. Biol. Chem.* **286**,
474   38329–38340 (2011).
475   17.   Hassinen, A. & Kellokumpu, S. Organizational Interplay of Golgi N-Glycosyltransferases
476   Involves Organelle Microenvironment-Dependent Transitions between Enzyme Homo- and
477   Heteromers. *J. Biol. Chem.* **289**, 26937–26948 (2014).
478   18.   Kellokumpu, S. Golgi pH, Ion and Redox Homeostasis: How Much Do They Really
479   Matter? *Front. Cell Dev. Biol.* **7**, (2019).

480   19.   Kornak, U. *et al.* Impaired glycosylation and cutis laxa caused by mutations in the
481   vesicular H + -ATPase subunit ATP6V0A2. *Nat. Genet.* **40**, 32–34 (2008).
482   20.   Morava, E. *et al.* Defective protein glycosylation in patients with cutis laxa syndrome.
483   *Eur. J. Hum. Genet.* **13**, 414–421 (2005).
484   21.   Jansen, E. J. R. *et al.* ATP6AP1 deficiency causes an immunodeficiency with hepatopathy,
485   cognitive impairment and abnormal protein glycosylation. *Nat. Commun.* **7**, 11600–11600
486   (2016).
487   22.   Rujano, M. A. *et al.* Mutations in the X-linked ATP6AP2 cause a glycosylation disorder
488   with autophagic defects. *J. Exp. Med.* **214**, 3707–3729 (2017).
489   23.   Cannata Serio, M. *et al.* Mutations in the V-ATPase Assembly Factor VMA21 Cause a
490   Congenital Disorder of Glycosylation With Autophagic Liver Disease. *Hepatology* **72**, 1968–1986
491   (2020).
492   24.   Jansen, J. C. *et al.* TMEM199 Deficiency Is a Disorder of Golgi Homeostasis Characterized
493   by Elevated Aminotransferases, Alkaline Phosphatase, and Cholesterol and Abnormal
494   Glycosylation. *Am. J. Hum. Genet.* **98**, 322–330 (2016).
495   25.   Jansen, J. C. *et al.* CCDC115 Deficiency Causes a Disorder of Golgi Homeostasis with
496   Abnormal Protein Glycosylation. *Am. J. Hum. Genet.* **98**, 310–321 (2016).
497   26.   Johnson, D. E., Ostrowski, P., Jaumouillé, V. & Grinstein, S. The position of lysosomes
498   within the cell determines their luminal pH. *J. Cell Biol.* **212**, 677 LP – 692 (2016).
499   27.   D'Amore, C. *et al.* Synthesis and Biological Characterization of a New Norbormide
500   Derived Bodipy FL-Conjugated Fluorescent Probe for Cell Imaging. *Front. Pharmacol.* **9**, (2018).
501   28.   Overly, C. C., Lee, K. D., Berthiaume, E. & Hollenbeck, P. J. Quantitative measurement of
502   intraorganelle pH in the endosomal-lysosomal pathway in neurons by using ratiometric imaging
503   with pyranine. *Proc. Natl. Acad. Sci.* **92**, 3156–3160 (1995).
504   29.   Liu, H. *et al.* Real-time monitoring of newly acidified organelles during autophagy
505   enabled by reaction-based BODIPY dyes. *Commun. Biol.* **2**, 1–11 (2019).
506   30.   Ma, L., Ouyang, Q., Werthmann, G. C., Thompson, H. M. & Morrow, E. M. Live-cell
507   Microscopy and Fluorescence-based Measurement of Luminal pH in Intracellular Organelles.
508   *Front. Cell Dev. Biol.* **5**, 71–71 (2017).
509   31.   Kim, J. H. *et al.* Dynamic measurement of the pH of the Golgi complex in living cells using
510   retrograde transport of the verotoxin receptor. *J. Cell Biol.* **134**, 1387–1399 (1996).
511   32.   Kim, J. H. *et al.* Noninvasive measurement of the pH of the endoplasmic reticulum at
512   rest and during calcium release. *Proc. Natl. Acad. Sci.* **95**, 2997–3002 (1998).
513   33.   Wu, M. M. *et al.* Organelle pH studies using targeted avidin and fluorescein–biotin.
514   *Chem. Biol.* **7**, 197–209 (2000).
515   34.   Miesenböck, G., De Angelis, D. A. & Rothman, J. E. Visualizing secretion and synaptic
516   transmission with pH-sensitive green fluorescent proteins. *Nature* **394**, 192–5 (1998).
517   35.   Mahon, M. J. pHluorin2: an enhanced, ratiometric, pH-sensitive green florescent
518   protein. *Adv. Biosci. Biotechnol.* **2**, 132–137 (2011).
519   36.   Ward, W. W., Prentice, H. J., Roth, A. F., Cody, C. W. & Reeves, S. C. Spectral
520   Perturbations of the Aequorea Green-Fluorescent Protein. *Photochem. Photobiol.* **35**, 803–808
521   (1982).
522   37.   Bizzarri, R. *et al.* Development of a Novel GFP-based Ratiometric Excitation and Emission
523   pH Indicator for Intracellular Studies. *Biophys. J.* **90**, 3300–3314 (2006).

524   38.   Hanson, G. T. *et al.* Green Fluorescent Protein Variants as Ratiometric Dual Emission pH
525   Sensors. 1. Structural Characterization and Preliminary Application. *Biochemistry* **41**, 15477–
526   15488 (2002).
527   39.   McAnaney, T. B., Park, E. S., Hanson, G. T., Remington, S. J. & Boxer, S. G. Green
528   Fluorescent Protein Variants as Ratiometric Dual Emission pH Sensors. 2. Excited-State
529   Dynamics. *Biochemistry* **41**, 15489–15494 (2002).
530   40.   Benink, H. A., McDougall, M. G., Klaubert, D. H. & Los, G. V. Direct pH measurements by
531   using subcellular targeting of 5(and 6-) carboxyseminaphthorhodafluor in mammalian cells.
532   *BioTechniques* **47**, 769–774 (2009).
533   41.   Wallrabe, H. & Periasamy, A. Imaging protein molecules using FRET and FLIM
534   microscopy. *Curr. Opin. Biotechnol.* **16**, 19–27 (2005).
535   42.   Jares-Erijman, E. A. & Jovin, T. M. FRET imaging. *Nat. Biotechnol.* **21**, 1387–1395 (2003).
536   43.   Schmitt, F.-J. *et al.* eGFP-pHsens as a highly sensitive fluorophore for cellular pH
537   determination by fluorescence lifetime imaging microscopy (FLIM). *Biochim. Biophys. Acta BBA*
538   *- Bioenerg.* **1837**, 1581–1593 (2014).
539   44.   Lin, H.-J., Herman, P. & Lakowicz, J. R. Fluorescence lifetime-resolved pH imaging of
540   living cells. *Cytometry A* **52A**, 77–89 (2003).
541   45.   Liu, Y., Kim, H.-R. & Heikal, A. A. Structural Basis of Fluorescence Fluctuation Dynamics
542   of Green Fluorescent Proteins in Acidic Environments. *J. Phys. Chem. B* **110**, 24138–24146
543   (2006).
544   46.   Cotlet, M. *et al.* Excited-State Dynamics in the Enhanced Green Fluorescent Protein
545   Mutant Probed by Picosecond Time-Resolved Single Photon Counting Spectroscopy. *J. Phys.*
546   *Chem. B* **105**, 4999–5006 (2001).
547   47.   Heikal, A. A., Hess, S. T. & Webb, W. W. Multiphoton molecular spectroscopy and
548   excited-state dynamics of enhanced green fluorescent protein (EGFP): acid–base specificity.
549   *Chem. Phys.* **274**, 37–55 (2001).
550   48.   Nakabayashi, T. *et al.* pH dependence of the fluorescence lifetime of enhanced yellow
551   fluorescent protein in solution and cells. *J. Photochem. Photobiol. Chem.* **235**, 65–71 (2012).
552   49.   Welch, L. G. & Munro, S. A tale of short tails, through thick and thin: investigating the
553   sorting mechanisms of Golgi enzymes. *FEBS Lett.* **593**, 2452–2465 (2019).
554   50.   Tie, H. C. *et al.* A novel imaging method for quantitative Golgi localization reveals
555   differential intra-Golgi trafficking of secretory cargoes. *Mol. Biol. Cell* **27**, 848–861 (2016).
556   51.   Boncompain, G. *et al.* Synchronization of secretory protein traffic in populations of cells.
557   *Nat. Methods* **9**, 493–493 (2012).
558   52.   Deka, C. *et al.* Analysis of fluorescence lifetime and quenching of FITC-conjugated
559   antibodies on cells by phase-sensitive flow cytometry. *Cytometry* **25**, 271–279 (1996).
560   53.   Huss, M. & Wieczorek, H. Inhibitors of V-ATPases: old and new players. *J. Exp. Biol.* **212**,
561   341 LP – 346 (2009).
562   54.   Forgac, M. Vacuolar ATPases: rotary proton pumps in physiology and pathophysiology.
563   *Nat. Rev. Mol. Cell Biol.* **8**, 917–917 (2007).
564   55.   Nishi, T. & Forgac, M. The vacuolar (H+)-ATPases--nature's most versatile proton pumps.
565   *Nat. Rev. Mol. Cell Biol.* **3**, 94–103 (2002).

566   56.   Galea, G., Bexiga, M. G., Panarella, A., O'Neill, E. D. & Simpson, J. C. A high-content
567   screening microscopy approach to dissect the role of Rab proteins in Golgi-to-ER retrograde
568   trafficking. *J. Cell Sci.* **128**, 2339–2349 (2015).
569   57.   Klausner, R. D., Donaldson, J. G. & Lippincott-Schwartz, J. Brefeldin A: insights into the
570   control of membrane traffic and organelle structure. *J. Cell Biol.* **116**, 1071–1080 (1992).
571   58.   Rzymski, T. *et al.* The unfolded protein response controls induction and activation of
572   ADAM17/TACE by severe hypoxia and ER stress. *Oncogene* **31**, 3621–3634 (2012).
573   59.   Chapnick, D. A., Bunker, E. & Liu, X. A biosensor for the activity of the "sheddase" TACE
574   (ADAM17) reveals novel and cell type–specific mechanisms of TACE activation. *Sci. Signal.* **8**,
575   rs1–rs1 (2015).
576   60.   Yan, Y., Zhang, J., Guo, J.-L., Huang, W. & Yang, Y.-Z. Multiple shRNA-mediated
577   knockdown of TACE reduces the malignancy of HeLa cells. *Cell Biol. Int.* **33**, 158–164 (2009).
578   61.   Verboogen, D. R. J., González Mancha, N., ter Beest, M. & van den Bogaart, G.
579   Fluorescence Lifetime Imaging Microscopy reveals rerouting of SNARE trafficking driving
580   dendritic cell activation. *eLife* **6**, (2017).
581   62.   Manderson, A. P., Kay, J. G., Hammond, L. A., Brown, D. L. & Stow, J. L.
582   Subcompartments of the macrophage recycling endosome direct the differential secretion of IL-
583   6 and TNFα. *J. Cell Biol.* **178**, 57–69 (2007).
584   63.   Eisenberg-Lerner, A. *et al.* Golgi organization is regulated by proteasomal degradation.
585   *Nat. Commun.* **11**, 409 (2020).
586   64.   Baumann, J. *et al.* Golgi stress–induced transcriptional changes mediated by MAPK
587   signaling and three ETS transcription factors regulate MCL1 splicing. *Mol. Biol. Cell* **29**, 42–52
588   (2018).
589   65.   Oku, M. *et al.* Novel Cis-acting Element GASE Regulates Transcriptional Induction by the
590   Golgi Stress Response. *Cell Struct. Funct.* **36**, 1–12 (2011).
591   66.   Taniguchi, M. *et al.* TFE3 Is a bHLH-ZIP-type Transcription Factor that Regulates the
592   Mammalian Golgi Stress Response. *Cell Struct. Funct.* **40**, 13–30 (2015).
593   67.   Reiling, J. H. *et al.* A CREB3–ARF4 signalling pathway mediates the response to Golgi
594   stress and susceptibility to pathogens. *Nat. Cell Biol.* **15**, 1473–1485 (2013).
595   68.   Sbodio, J. I., Snyder, S. H. & Paul, B. D. Golgi stress response reprograms cysteine
596   metabolism to confer cytoprotection in Huntington's disease. *Proc. Natl. Acad. Sci.* **115**, 780–
597   785 (2018).
598   69.   Taniguchi, M. *et al.* MLX Is a Transcriptional Repressor of the Mammalian Golgi Stress
599   Response. *Cell Struct. Funct.* **41**, 93–104 (2016).
600   70.   Stransky, L., Cotter, K. & Forgac, M. The Function of V-ATPases in Cancer. *Physiol. Rev.*
601   **96**, 1071–1091 (2016).
602   71.   Wolfe, D. M. *et al.* Autophagy failure in Alzheimer's disease and the role of defective
603   lysosomal acidification. *Eur. J. Neurosci.* **37**, 1949–1961 (2013).
604   72.   Koh, J.-Y., Kim, H. N., Hwang, J. J., Kim, Y.-H. & Park, S. E. Lysosomal dysfunction in
605   proteinopathic neurodegenerative disorders: possible therapeutic roles of cAMP and zinc. *Mol.*
606   *Brain* **12**, 18 (2019).
607   73.   Dehay, B. *et al.* Loss of P-type ATPase ATP13A2/PARK9 function induces general
608   lysosomal deficiency and leads to Parkinson disease neurodegeneration. *Proc. Natl. Acad. Sci.*
609   **109**, 9611–9616 (2012).

610   74.   Jinn, S. *et al.* TMEM175 deficiency impairs lysosomal and mitochondrial function and
611   increases α-synuclein aggregation. *Proc. Natl. Acad. Sci.* **114**, 2389–2394 (2017).
612   75.   Fernandez-Mosquera, L. *et al.* Mitochondrial respiratory chain deficiency inhibits
613   lysosomal hydrolysis. *Autophagy* **15**, 1572–1591 (2019).
614   76.   Bagh, M. B. *et al.* Misrouting of v-ATPase subunit V0a1 dysregulates lysosomal
615   acidification in a neurodegenerative lysosomal storage disease model. *Nat. Commun.* **8**, 14612
616   (2017).
617   77.   Falcón-Pérez, J. M., Nazarian, R., Sabatti, C. & Dell'Angelica, E. C. Distribution and
618   dynamics of Lamp1-containing endocytic organelles in fibroblasts deficient in BLOC-3. *J. Cell Sci.*
619   **118**, 5243–5255 (2005).
620   78.   Warren, S. C. *et al.* Rapid Global Fitting of Large Fluorescence Lifetime Imaging
621   Microscopy Datasets. *PLOS ONE* **8**, e70687 (2013).
622   79.   Virtanen, P. *et al.* SciPy 1.0: fundamental algorithms for scientific computing in Python.
623   *Nat. Methods* **17**, 261–272 (2020).
624   80.   Ritz, C., Baty, F., Streibig, J. C. & Gerhard, D. Dose-Response Analysis Using R. *PLOS ONE*
625   **10**, e0146021 (2015).
626   81.   Wickham, H. *ggplot2: Elegant Graphics for Data Analysis*. (Springer-Verlag New York,
627   2016).
628